Carbon 172 (2021) 214–227

Contents lists available at ScienceDirect

Carbon

journal homepage: www.elsevier.com/locate/carbon

Research Article

Monitoring the thermally induced transition from sp^3-hybridized into sp^2-hybridized carbons

Dominique B. Schüpfer [a, *], Felix Badaczewski [b], Jan Peilstöcker [b], Juan Manuel Guerra-Castro [c], Hwirim Shim [d, e], Saleh Firoozabadi [f], Andreas Beyer [f], Kerstin Volz [f], Volker Presser [d, e], Christian Heiliger [c], Bernd Smarsly [b], Peter J. Klar [a]

[a] Institute of Experimental Physics I and Center for Materials Research (LaMa), Justus Liebig University Giessen, 35392, Giessen, Germany
[b] Institute of Physical Chemistry and Center for Materials Research (LaMa), Justus Liebig University Giessen, 35392, Giessen, Germany
[c] Institute for Theoretical Physics and Center for Materials Research (LaMa), Justus Liebig University Giessen, 35392, Giessen, Germany
[d] INM - Leibniz Institute for New Materials, 66123, Saarbrücken, Germany
[e] Department of Materials Science and Engineering, Saarland University, 66123, Saarbrücken, Germany
[f] Department of Physics and Materials Sciences Center (WZMW), Philipps University Marburg, 35032, Marburg, Germany

ARTICLE INFO

Article history:
Received 21 July 2020
Received in revised form
17 September 2020
Accepted 21 September 2020
Available online 28 September 2020

Keywords:
Amorphous carbon
Adamantane
Carbon onions
Nanodiamond
Carbon characterization
Raman spectroscopy

ABSTRACT

The preparation of carbons for technical applications is typically based on a treatment of a precursor, which is transformed into the carbon phase with the desired structural properties. During such treatment the material passes through several different structural stages, for example, starting from precursor molecules via an amorphous phase into crystalline-like phases. While the structure of non-graphitic and graphitic carbon has been well studied, the transformation stages from molecular to amorphous and non-graphitic carbon are still not fully understood. Disordered carbon often contains a mixture of sp^3-, sp^2-and sp^1-hybridized bonds, whose analysis is difficult to interpret. We systematically address this issue by studying the transformation of purely sp^3-hybridized carbons, that is, nanodiamond and adamantane, into sp^2-hybridized non-graphitic and graphitic carbon. The precursor materials are thermally treated at different temperatures and the transformation stages are monitored. We employ Raman spectroscopy, WAXS and TEM to characterize the structural changes. We correlate the intensities and positions of the Raman bands with the lateral crystallite size L_a estimated by WAXS analysis. The behavior of the D and G Raman bands characteristic for sp^2-type material formed by transforming the sp^3-hybridized precursors into non-graphitic and graphitic carbon agrees well with that observed using sp^2-structured precursors.

1. Introduction

Carbon materials are widely used in energy storage systems, for example, as components in supercapacitors or as electrodes in Li-ion batteries [1,2]. Especially carbons consisting of parallelly stacked graphene sheets without order in the third dimension are well suited for those applications [3]. A good control of the structural properties of the carbon material employed is essential as these properties determine the processes and reactions taking place in the material's interior and at its surface during device operation. Thus, the structural properties also contribute significantly to the resulting device performance. Structural parameters of particular interest include the stacking height, stacking order, defect content, and the lateral extent of the graphene layers. Non-graphitic and graphitic carbons are well understood, whereas the structural evolution in the first stages of the transformation process from a precursor material to the intermediate carbon-rich materials has remained incompletely characterized. It is important to identify the sequence of structural changes during heating, in particular, as the same carbon material may be prepared with different kinds of precursors. In contrast to the crystalline samples, amorphous carbon consists of a mixture of sp^3-, sp^2-and sp^1-hybridized entities. These bonds in amorphous carbon are broken and rearranged during annealing in the low-temperature regime. In the transition phase between amorphous and non-graphitic carbons, small

* Corresponding author.
E-mail address: dominique.b.schuepfer@exp1.physik.uni-giessen.de (D.B. Schüpfer).

https://doi.org/10.1016/j.carbon.2020.09.063

hexagonal rings are assumed to slowly fuse, forming an, at first, disordered network. The network transforms into graphene-like sheets, which increase in lateral size with increasing annealing temperature yielding non-graphitic carbon without stacking order or even graphitic carbon with ordered stacking of the graphene-like sheets.

We demonstrated in a recent study that Raman spectroscopy can be used to monitor the structural transformation from different sp^2-hybridized precursors, i.e., pitches and resins, into graphitic carbons [4]. We found that the transformation process passes through four structurally different stages during heat-treatment. The annealing at first yields amorphous carbon with crystallite sizes $L_a < 2$ nm, a transition region with L_a between 2 nm and 4 nm, non-graphitic carbon with $L_a > 4$ nm and graphitic carbon with $L_a > 20$ nm. The behavior of the D, G, and 2D Raman bands found for non-graphitic and graphitic carbon can be modeled by line shape models based on the electronic band structure and the phonon dispersion relations of the ideal infinitely large crystalline systems (see Ref. [4]). In particular, it is found that the end of the transformation chain is to a first approximation independent of the type of sp^2-hybridized precursor used, i.e., different starting points (precursors) lead to the same product (graphitic carbon). So far, the focus of research was on the transformation from sp^2-type precursors to sp^2-type graphitic carbon. Typical precursors used for synthesizing graphitic carbon are, for example, pitches [4,5], whereas the use of resins results in non-graphitic carbon [6,7]. Furthermore, heat-treated biomass waste, which is structurally somewhat ill-defined, is also under investigation, for example, as carbonaceous electrode material in applications like Li-ion batteries [8,9]. Nanodiamond up to now is the only pure sp^3-hybridized precursor which has been used in studies of thermal synthesis of carbon materials [10–13]. However, the transition phase between nanodiamond and crystalline carbon consisting of a mixed phase of sp^2 and sp^3-hybridized structures has not been studied in detail yet. Adamantane employed in this work is the second example of a well defined sp^3-hybridized precursor for carbon materials. Studies of well defined sp^3-structured precursors and of their transformation into carbons by heat-treatment may complement the vast studies of sp^2-hybridized precursors. In particular, such investigations will help to unravel the microscopic processes occurring at the intermediate stages of the structural transformation. Fundamental questions to ask are: What happens, if sp^3-hybridized precursors are used instead of sp^2-hybridized materials? How does the sp^3-network of the precursor transform into the sp^2-network of graphitic carbon and what are the corresponding changes of the Raman spectra? We seek the answers by studying, on the one hand, the heat-induced transformation of nanodiamonds via carbon onions into non-graphitic carbon [10,12,14,15], and, on the other hand, that of adamantane, the smallest diamond-like molecule, into non-graphitic carbon. Both, nanodiamonds as well as adamantane molecules are ideal precursors for this purpose as they exhibit sp^3-networks only.

2. Experimental part

We prepared series of samples by heat-treatment of the sp^3-hybridized precursors, namely commercially available nanodiamond and adamantane. The nanodiamonds (Nabond Technologies) were heat-treated at temperatures up to 3000 °C. The adamantane-based series of samples was prepared by annealing commercially available adamantane (Sigma-Aldrich) at various temperatures up to 525 °C in a quartz ampulla under vacuum condition. Higher temperatures were not achievable due to the high pressure arising in the ampulla during annealing. For comparison, we also studied series of carbon samples obtained from sp^2-type precursors, i.e., a low-softening point pitch with a softening point at 70 °C (LSPP-70) prepared from polycyclic aromatic hydrocarbons (PAH) and a heat-treated resin prepared from a resol precursor. These precursors were heat-treated at different temperatures up to 3000 °C in Ar atmosphere, to yield samples representing the different stages of the carbonization process. The pitch precuror is graphitizable, whereas the resin precursor is non-graphitizable. The samples are labeled by the heat-treatment temperature; the label 20 °C indicates the untreated samples. More details about the annealing process and its parameters can be found elsewhere [16].

WAXS data were collected with a PANalytical X'Pert Pro powder diffractometer in Bragg-Brentano geometry using Cu K_α radiation with a wavelength $\lambda = 1.5418$ Å. The sample under study was crushed manually and then flattened on a sample holder to a thickness of 1 mm. The measurements were performed in the range of $10° < 2\theta < 100°$ and an acquisition time of 8 s/step. The carbon samples were measured with a step width of 0.1° to account for their higher crystallinity and therefore sharper reflection signals. No background intensity was subtracted from the experimental WAXS data.

The WAXS data were fitted by applying the algorithm developed by Ruland and Smarsly [17] yielding, amongst other parameters, the average lateral size L_a of the graphene-like sheets. The WAXS data of pitch-based samples heat-treated at temperatures $\geq$ 2800 °C show (*hkl*)-reflections, indicating the onset of graphitization. These data cannot be fitted by the algorithm as the underlying model does not account for (*hkl*)-reflections. Therefore, the crystallite size was estimated by Scherrer's formula for those samples [18]. The full-width at half-maximum (FWHM) of their (110) reflection was determined using a Gaussian profile. The (110) reflection was chosen, because it does not strongly overlap with other reflections, in contrast to the (100) reflection. The disorder within the lattice was neglected during this approach. The obtained values possess a somewhat larger uncertainty than the WAXS data for lower heat-treatment temperatures, as the (110)-reflection cannot be separated unambiguously from neighboring reflections and from the non-linear background. In the case of the nanodiamond sample series annealed up to 1300 °C, the nanodiamond reflections dominate the diffraction curve and Scherrer's formula is used to estimate the crystallite sizes of the diamond core. The WAXS data for the sample series including the nanodiamonds and carbon onions are shown in the Supporting Information (SI) Fig. S3.

The Raman spectra were recorded with a Renishaw inVia Raman spectrometer with a focal length of 250 mm combined with a Leica optical microscope. The Raman system works in backscattering geometry at room temperature. Excitation light with a wavelength of 325 nm was focused onto the sample by either a 20× or a 40× microscope objective. The laser focus was about 4 μm in diameter on the sample. The scattered light was collected by the microscope objective and then dispersed by the spectrometer employing a grating with 1800 grooves per millimeter before it was detected by a charge-coupled device detector (CCD). The spectral resolution of the Raman system was about 1.5 cm^{-1}. The exposure time was about 30 s for each acquisition and 5 to 10 acquisitions were accumulated to obtain a sample's Raman spectrum in the range from 1000 cm^{-1}–3200 cm^{-1} with a good signal-to-noise ratio. The laser power was kept as low as possible to avoid structural damage of the samples. Laser power as low as about 0.3 mW–0.7 mW was used for the nanodiamonds due to their high Raman scattering cross-sections. However, in the case of the pitches, in particular, those prepared at low temperatures, laser powers up to 7 mW had to be used to obtain good quality spectra. None of the samples studied showed signs of deterioration after exposure to the laser light.

Transmission electron microscopy (TEM) images of the nanodiamond and carbon onions were obtained from using a JEOL JEM-2100F system with an operating voltage of 200 kV. The carbon samples were dispersed in ethanol and then tip-sonicated for 30 s. The dispersion was drop casted on a TEM copper grid with a lacy carbon film.

For TEM investigations of the adamantane-based-samples, a dual beam scanning electron microscope focused ion beam (FIB) machine (JEOL JIB-4601F, JEOL Ltd., Tokyo, Japan) was used to prepare an electron transparent lamella. A double-aberration-corrected JEOL 2200FS scanning transmission electron microscope operating at 200 kV was used to perform both high resolution transmission electron microscopy (HRTEM) and electron energy loss spectroscopy (EELS). The EELS investigations were conducted at scanning mode and with the help of an in column energy filter. However, the HRTEM investigations were performed at conventional TEM mode. A condenser aperture resulting in a convergent angle of 22 mrad was used for the EELS measurements. In addition, a collection angle of 10 mrad was obtained by applying an entrance aperture prior to the spectrometer. The resulting energy resolution of 1.1 eV could be achieved by measurement of zero loss full with at half-maximum.

Furthermore, band structure and phonon dispersion of ideal diamond were calculated by density functional theory. The software QUANTUM ESPRESSO [19,20] was employed for this purpose. The calculated bandstructure and phonon dispersion served as input parameters for the Campbell-Fauchet modelling of the size dependence of the lineshape and position of the nanodiamond Raman signal [21,22].

3. Results and discussion

3.1. Raman spectra of the nanodiamond-based and adamantane-based heat-treated samples

Fig. 1 shows an overview of the Raman spectra and corresponding transmission electron microscopy (TEM) images of the nanodiamond-based series of samples heat-treated up to 3000 °C. The TEM images reveal that with increasing heat-treatment temperature, the structure of the nanodiamonds changes. Starting from the nanodiamond surface, shell-like layers are formed around its core. The number of layers of the shell increases as the nanodiamond-like core decreases with increasing temperature. This gives rise to the onion-like appearance of the nanoparticles annealed at higher temperatures, finally forming carbon onions [12,14,15]. This structural transformation also has an impact on the Raman spectra.

At low heat-treatment temperatures up to 700 °C, the prominent Raman signals of the spectra at 1325 cm^{-1} and at about 1640 cm^{-1} are commonly observed in Raman spectra of nanodiamond samples. The former band at 1325 cm^{-1} represents the one-phonon Raman process with the triply degenerated optical phonons at the Γ-point [23,24]. The origin of the latter Raman band remains disputed. Competing explanations can be found in the literature. In 1963, Birman suggested a two-phonon Raman process involving two transverse acoustic phonons of the phonon dispersion of diamond [23]. In the late 1990s and 2000s other explanations appeared: trigonal bond arrangements stiffened by the tetrahedral environment [11], olefinic chains [25], a mixture of sp^2 and sp^3-bonds [13] and dumbbell defects [26]. The most likely explanation was given by Mochalin et al. in 2009 based on oxidation experiments. It states that the broad Raman band at 1640 cm^{-1} consists of contributions from O–H bending modes and, in addition, contains signal contributions from sp^2-hybridized carbon at 1590 cm^{-1} as well as a signal arising from C=O stretching modes at 1740 cm^{-1} [27,28].

The additional broad signal or extended tail on the low-frequency side of the nanodiamond signal between 1000 cm^{-1} and 1300 cm^{-1} is considered to arise from an overlap of different contributions. A contribution between about 1050 cm^{-1} and 1100 cm^{-1} is possibly related to the vibrational density of states of tetrahedrally bonded amorphous carbon. This band is enhanced when the laser excitation is in resonance with the σ-states [29,30] and referred to as “T band” [31,32]. A second contribution at about 1150 cm^{-1} is assigned to *trans*-polyacetylene (TPA) forming at grain boundaries [32–34]. The third contribution at about 1250 cm^{-1} corresponds to the phonon density of states of diamond and may arise due to disorder in the small nanodiamond particles which form in the samples prepared at low heat-treatment temperatures [13,26].

The Raman spectra of samples treated at temperatures of 1300 °C and higher are characteristic for sp^2-hybridized carbons transforming from the amorphous phase into crystalline non-graphitic or graphitic carbon. Note that non-graphitic carbon possess defined graphene layers, which exhibit 2D crystalline order. The prominent features in the Raman spectra are the so called D and G Raman bands at about 1400 cm^{-1} and 1580 cm^{-1}, respectively. In graphene, the G Raman mode corresponds to a one-phonon Raman process of an LO phonon from the center of the Brillouin-zone, whereas the D mode corresponds to higher-order resonant Raman processes involving a phonon close to the K or K’ point of the Brillouin-zone and scattering by a structural defect. This notation is applied even in the amorphous phase as the two Raman bands observed for amorphous carbon evolve into the graphene-like signals on annealing [35,36]. The evolution of the Raman spectra with an increasing heat-treatment temperature between 1300 °C and 3000 °C observed from our data aligns with the literature. At 1300 °C, the Raman spectrum shows broad and overlapping D and G bands. Both bands sharpen with increasing heat-treatment temperature. The D band intensity drops significantly and is almost zero at 3000 °C while the G band intensity changes much less. This behavior shows that the defect concentration decreases and the degree of order increases during annealing.

Whether the crystalline phase formed at the highest temperatures is non-graphitic or graphitic carbon can be decided by an analysis of the shape of the 2D Raman signal. As defined by the International Union of Pure and Applied Chemistry (IUPAC), non-graphitic (or turbostratic) carbon consists of stacks of graphene layers, which are rotated with respect to each other and severely vary in their interlayer distances within one stack and therefore, show no strict periodic order in the third dimension [3]. Because of the large distance between the graphene layers in non-graphitic carbon, there is only a weak interaction between them. Thus, the 2D Raman signal of non-graphitic carbon consists of one Raman band only and that of graphitic carbon consists of at least two overlapping bands [37–42]. A sharp 2D signal typically is observable only for the samples annealed at temperatures larger than 1800 °C. A corresponding series of Raman spectra prepared from the nanodiamond precursor at various heat-treatment temperatures is shown in the Supporting Information (SI) in Fig. S1. All samples prepared from the nanodiamond precursor can be classified as non-graphitic carbon. Only the sample prepared at 3000 °C is on the verge of becoming graphitic. This interpretation is in line with WAXS data on these samples, revealing (*hkl*) reflections for 3000 °C, which is characteristic for graphitic carbons (see SI Fig. S3).

We will now consider the transition region between nanodiamond-like and graphene-like spectra represented by the two Raman spectra taken on different particles of the sample heat-treated at 1100 °C labeled I and II in Fig. 1. The Raman spectrum I

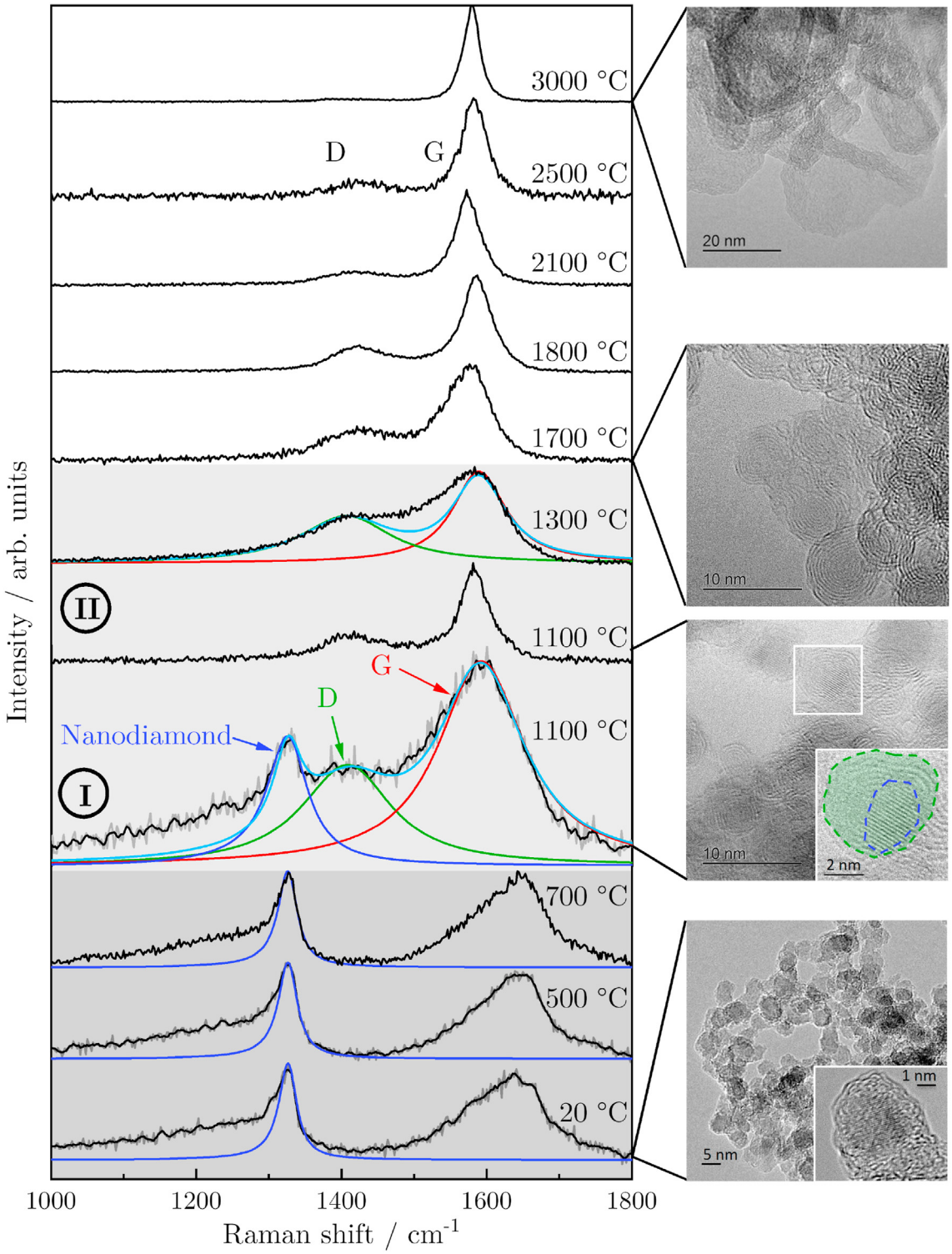

Fig. 1. Overview of the Raman spectra of the series of nanodiamond-based samples heat-treated at different temperatures. The excitation laser wavelength was 325 nm. The Raman spectra of the samples labeled at 20 °C, 500 °C, and 1100 °C are smoothed (average over 10 data points), because of a low signal-to-noise-ratio. Back lines represent the smoothed curves, and grey lines show the original spectra. The transmission electron micrographs on the right reveal the onion-like structure of the carbons. (A colour version of this figure can be viewed online.)

reveals simultaneously nanodiamond-like Raman bands and the so called D and G Raman bands of amorphous carbon. In the probed spot, the sample seems to consist of coexisting sp^2-and sp^3-structured networks. In contrast, Raman spectrum II taken in a neighboring spot of the same sample does not reveal any nanodiamond-like features. It only exhibits a broad feature in the spectral region of the D Raman band and a rather narrow G Raman band. Spectrum II is thus already typical for amorphous carbon. Apparently, at 1100 °C, areas of the sample showing a mixture of sp^2-and sp^3-hybridized material networks (spectrum I) coexist with neighboring areas

already dominated by sp^2-type networks (spectrum II). Also, the T band has vanished in spectrum II, whereas it is still visible in spectrum I. These findings indicate the transformation from sp^3-to sp^2-hybridized carbon takes place in a narrow temperature window and, second, that it does not need to occur homogeneously. A possible reason might be that the transformation temperature depends on particle size and varies slightly throughout the size distribution of the nanodiamond starting material.

The line shape of Raman bands in nanostructures is indicative of the particle size. This phonon confinement effect may be successfully described by the model introduced by Campbell and Fauchet [22,43]. The model may be used to estimate the characteristic nanoparticle size from the nanoparticle's Raman spectrum. We employ this approach here to the nanodiamond-like signal at 1325 cm^{-1} as well as for the G and D-like modes at 1580 cm^{-1} and 1400 cm^{-1}, respectively. We have demonstrated recently for sp^2-hybridized carbons, that this approach applied to the D and G mode yields average lateral extensions L_a of the graphene-like nanosheets of the material, which is in concordance with the values obtained by the WAXS analysis. The line shape modelling requires the knowledge of the phonon dispersions of the corresponding bulk material, i.e., diamond and graphene. We have derived those dispersions by density functional theory. The phonon dispersions calculated and the equations used are given in the SI in Fig. S2. Exemplarily, we show the results for the sample annealed at 1100 °C in Fig. 1. The profiles of the D and G band as well as the nanodiamond signal at 1325 cm^{-1} are fitted with the Campbell-Fauchet model. The fitting yields L_a values of 4 nm for the D and G band and of 3.4 nm in case of the nanodiamond band. These findings are in good agreement with the transmission electron micrograph analysis shown on the right of Fig. 1. In case of the 1300 °C sample the nanodiamond Raman signal at 1325 cm^{-1} disappears, but traces of signals typical for nanodiamond between 1000 cm^{-1} and 1300 cm^{-1} are still present. Unfortunately, the X-ray diffraction (XRD) signals of the nanodiamonds ((111) reflection) and that of the emerging graphene layers ((10) reflection) substantially overlap in the range of $s = 4.8\ nm^{-1}$ (Fig. S3 in the SI). Hence, the calculation of L_a from XRD data was not possible for this temperature, and $L_a = 4.5$ nm was thus estimated based on the Raman spectrum (Fig. 1). Employing the Campbell-Fauchet model for the nanodiamond Raman band of the pristine nanodiamonds and those heat-treated at 500 °C and 700 °C, yielded corresponding crystallite sizes of 3.5 nm, 3.5 nm and 3.4 nm. This result is in agreement with the analysis of the linewidths of the corresponding diamond (111) XRD reflections using Scherrer's formula providing crystallite sizes, which are equivalent to the domain sizes resulting from the Campbell and Fauchet model.

Thus, the interpretation of the Raman spectra, in particular in the transition region, is in full accordance with the transmission electron micrographs depicted in Fig. 1. The analysis of the transformation of the carbon onions by TEM images is discussed in more detail by Zeiger et al. [12,14,15]. Samples heat-treated up to 700 °C are still nanodiamond-like. The nanoparticles show prominent diamond-like cores with few structural deviations close to their surfaces. After annealing at 1100 °C, most particles consist of a nanodiamond core surrounded by a sp^2-hybridized carbon shell, i.e., sp^3-like bonds turn into sp^2 bonds starting from the outside of the nanodiamonds leading to the carbon onion structure. With the increasing heat-treatment temperature up to 1700 °C and even higher, the sp^2-shell grows at the expense of the shrinking sp^3-structured core of the corresponding nanoparticle [10,12].

We will now discuss the heat-treatment results employing the second sp^3-type precursor. Adamantane as a molecular precursor is structurally even better defined than nanodiamond as the pristine molecule ensemble does not exhibit any size distribution in contrast to a nanoparticle ensemble. The Raman spectra of the adamantane-based series of samples are shown in Fig. 2. We annealed samples at 400 °C, 450 °C, 475 °C, 500 °C, and 525 °C. At heat-treatment temperatures up to 450 °C, the adamantane powder melted and evaporated during heat-treatment and condensed again on cooling. Both products obtained kept the white color of the pristine adamantane powder. The situation changed for the sample annealed at 475 °C and higher. In these cases, the products obtained after cooling down were of black color. Staying in the molecular picture, it means that the adamantane molecules have reacted at these higher temperatures and formed various other molecules of larger size.

The differences in the products obtained at heat-treatment temperatures, on the one hand, of $\leq$ 450 °C and, on the other hand, of $\geq$ 475 °C are also reflected in the corresponding Raman spectra. The Raman spectra of the samples heat-treated at 400 °C and 450 °C show no change compared to the Raman spectrum of pristine adamantane (the Raman spectrum of the 400 °C sample is omitted in the figure). In contrast, the Raman spectra of the samples annealed at 475 °C and above are different from that of adamantane. The sharp adamantane signals have vanished and two broad features appeared instead in the spectral range between 1000 cm^{-1} and 1800 cm^{-1}. The broader feature centered at 1372 cm^{-1} seems to consist of several overlapping contributions, whereas the stronger and narrower feature centered at 1617 cm^{-1} seems to comprise one broadened band only. The two broad features arise from the different molecules formed during annealing, whose Raman bands are now contributing to the measured spectrum. By comparison with the Raman spectra of candidate molecules, we will attempt to explain the Raman spectrum measured. The Raman band at 1617 cm^{-1} has been assigned to coronene and similar polycyclic aromatic hydrocarbons (PAH) [44]. For comparison, Raman spectra of coronene and pyrene using an excitation wavelength of 325 nm are shown in the SI in Fig. S4.

A comparison with the Raman spectra of small PAHs in SI Fig. S4, suggests that the feature at lower wavenumbers is due to an A_{1g} Raman mode at 1372 cm^{-1} of small sp^2-hybridized molecules such as pyrene. The shoulder at 1245 cm^{-1} might originate from A_{1g} Raman modes of molecules like coronene or larger PAHs [44]. Contributions in the range from 1400 cm^{-1}–1500 cm^{-1} probably are due to vibrations of residual diamondoid-like molecules such as adamantane, triamantane, or diamondoid dimers [45] and chain-like carbon structures like polyethylene.

The spectral appearance of the spectra of the samples annealed at 475 °C and above with their two broad main Raman features centered at 1372 cm^{-1} and 1617 cm^{-1} resembles that of the amorphous carbon phase with its broad overlapping D and G band. Thus, we consider the broad features pre-stages of the D and G Raman bands in what follows. The characteristic sizes L_a of the graphene-like units within the samples are very likely still below 1 nm as the molecular character of the spectral features is still clearly visible.

This hypothesis is further corroborated by the TEM and electron energy loss spectroscopy (EELS) analysis. A high-angle annular dark field image of the prepared TEM lamella is shown in Fig. 3a) illustrating the position of the sample along with the amorphous protection layer deposited during the sample preparation. For the EELS analysis, a relatively thin area of the carbon protection layer was used as an amorphous reference spectrum. A carbon K-edge EELS spectrum from the reference and three different areas of the sample are plotted in Fig. 3b). All the spectra are taken while the electron beam was scanned over a region of 6 × 6 nm^2 on the sample. The defined peak centered at an energy of 325 eV, which is not seen in the EELS spectrum of the reference, is indicative for the existence of sp^3-hybridized carbon in the adamantane-based

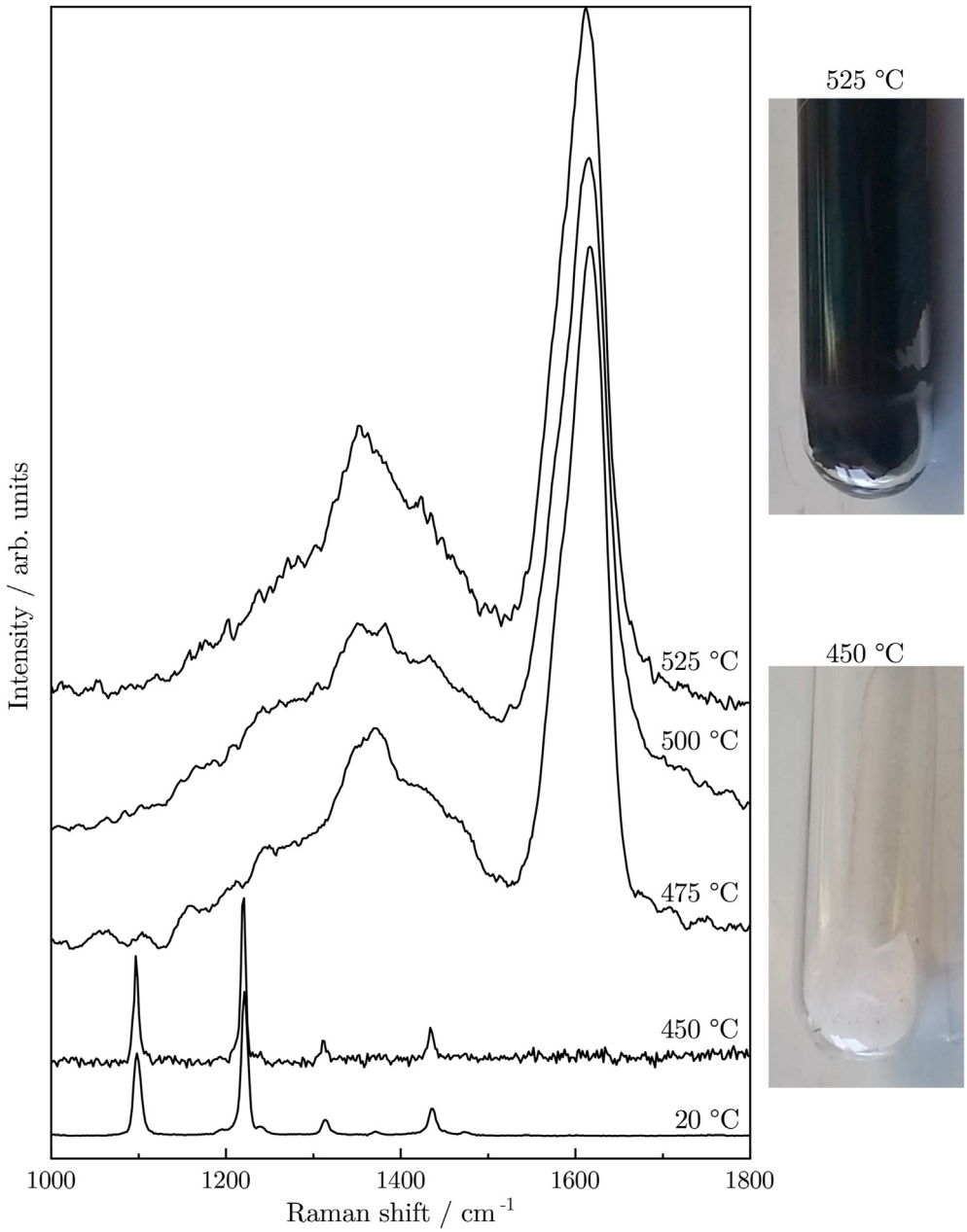

Fig. 2. Overview of the Raman spectra (325 nm laser line) of the adamantane-based series of samples annealed at different temperatures. The transition from the pristine adamantane precursor into a product consisting of various hydrocarbons with sp^2 and sp^3-bonds (in particular, chain-like and polycyclic aromatic hydrocarbons) takes place at heat-treatment temperatures of 475 °C and above. The corresponding Raman spectra exhibit two main features similar to those observed in the Raman spectra of amorphous carbons. On the right side, photographs of the samples are shown. (A colour version of this figure can be viewed online.)

sample heat-treated at 525 °C [46]. In the HRTEM images neither of the amorphous carbon reference nor of the adamantane-based sample nanoparticles can be discerned, showing that the sample is indeed rather molecule-like. HRTEM images along with corresponding Fast Fourier transforms (FFT) as an inset are illustrated in Fig. 3c) and d) for the amorphous reference and for the sample, respectively. The radial distributions derived from the FFTs in Fig. 3c) and d) are depicted in Fig. 3e). The radial distribution of the sample exhibits a more pronounced peak structure than the reference measurement. This finding suggests that the bond length distribution is sharper than in the reference sample indicating an onset of crystallinity. This is in line with the presence of small, still molecule-like nanometer-sized particles in this measurement area of 75 × 75 nm^2.

3.2. Comparison of G and D band-like features in samples derived from sp^2- and sp^3-hybridized precursors

In what follows, we will compare the sp^2-hybridized products, i.e., amorphous carbon and non-graphitic carbon, obtained from sp^3-type precursors and sp^2-structured precursors in terms of their Raman fingerprints. As a reference, we modeled the positions of the G and D Raman bands of graphene nanosheets in dependence on their lateral size L_a. The theoretical curves were derived from phonon dispersions of ideal graphene calculated by density functional theory in combination with the Campbell-Fauchet model of phonon confinement [4]. Furthermore, we compare, as a function of L_a, the ratio of the intensity I_D of the D Raman band to the intensity I_G of the G Raman band of the samples. In case of the

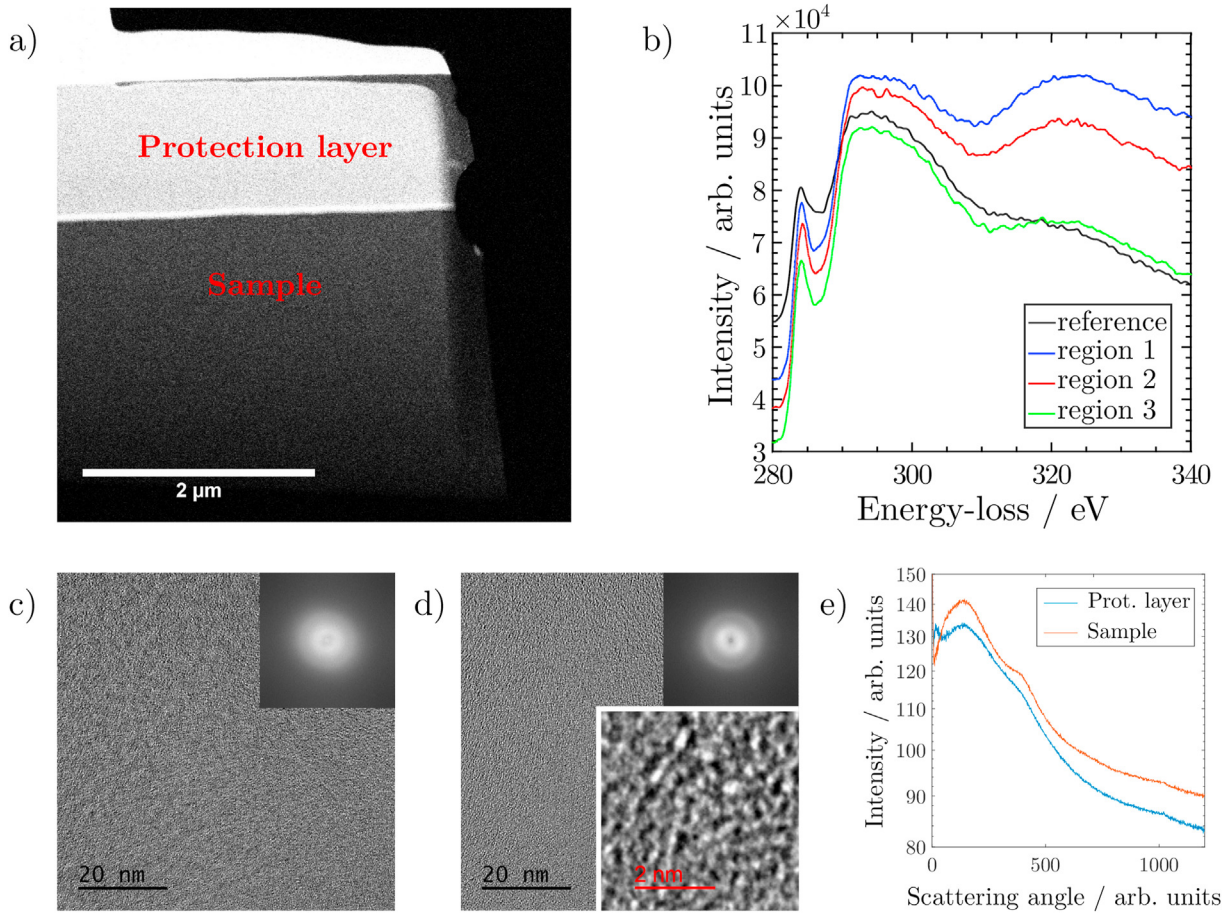

Fig. 3. HRTEM and EELS analysis, a) an overview of electron transparent lamella depicting the position of amorphous protection layer and sample area, b) carbon k-edge EELS spectrum from the amorphous reference and sample, c) and d) the HRTEM images at the position of amorphous reference and sample area, e) radial distribution of the FFTs shown in panels (c) and (d). (A colour version of this figure can be viewed online.)

samples derived from sp^3-hybridized precursors, we focus on the nanodiamond-based samples heat-treated at 1100 °C, 1300 °C, 1700 °C, 1800 °C, 2100 °C, 2500 °C, and 3000 °C as corresponding L_a values were accessible by WAXS and TEM analysis. The adamantane-based samples heat-treated at 475 °C, 500 °C, and 525 °C were also included in the analysis, but the size L_a could only be estimated. As reference materials derived from sp^2-hybridized precursors, we employed a series of heat-treated samples based on a soft pitch (LSPP-70, low softening point of 70 °C) and a resole-based resin. The lateral sizes of these samples were determined by analyzing the corresponding WAXS data [17] (SI Fig. S3).

Fig. 4a) and b) show plots of the G band and D band positions as a function of L_a extracted from the Raman spectra of the sample series recorded at 325 nm excitation. Furthermore, the two graphs show corresponding theoretical reference curves derived in the framework of the phonon confinement model introduced recently [4]. In case of the G Raman band, the pitch and resin-based samples show the same trend, i.e., the G band position increases with decreasing L_a from about 1580 cm^{-1} to about 1620 cm^{-1}. This blue-shift of the G band position is reproduced by the model down to a size L_a of about 2 nm. At smaller sizes, the theory deviates from the experimental sp^2-hybridized reference data. However, this is anticipated as the model is based on a perturbational treatment of crystalline graphene and is prone to fail when the samples become molecule-like. The overall agreement between the data points originating from samples prepared by sp^3- and sp^2-based precursors is reasonable and yields further clarifications. The G band positions of the carbon onion samples based on sp^3-hybridized nanodiamond as precursor match the data of the pitch and resin-based sp^2-type samples in the range of large $L_a > 4$ nm, i.e., suggesting that they are indeed structurally similar. These data originate from samples heat-treated at temperatures of 1100 °C and above. In contrast, the data of the nanodiamond-based carbon onions heat-treated at lower temperatures all exhibit a Raman band at 1640 cm^{-1}. The band position deviates from the G-band of the sp^2-hybridized reference samples of comparable size by more than 20 cm^{-1} (data points not shown in the figure to avoid mixing up typical nanodiamond features and signals of sp^2-structures). Thus, this band at 1640 cm^{-1} in the Raman spectra of the nanodiamond-derived samples with $L_a < 4$ nm does not correspond to the G band, but rather should be assigned to a mixed signal consisting mainly of contributions of O–H and C=O modes with only minor contributions of sp^2-hybridized carbon or to two-phonon signals of nanodiamond in concordance with literature. The G band positions of the adamantane-based samples obtained by heat-treatment at temperatures of 475 °C and above, on the other hand, agree nicely with the experimental data on the pitch and resin-based samples with L_a values smaller than 1 nm and are also in concordance with the TEM analysis given above. This size range also agrees well with the findings of Oya et al., who also heat-treated adamantane, and suggested a pitch-like structure of the products on the basis of XRD and nuclear magnetic resonance spectroscopy data [47]. The sample annealed at 475 °C exhibits the highest Raman shift at 1617 cm^{-1} whereas for that annealed at 525

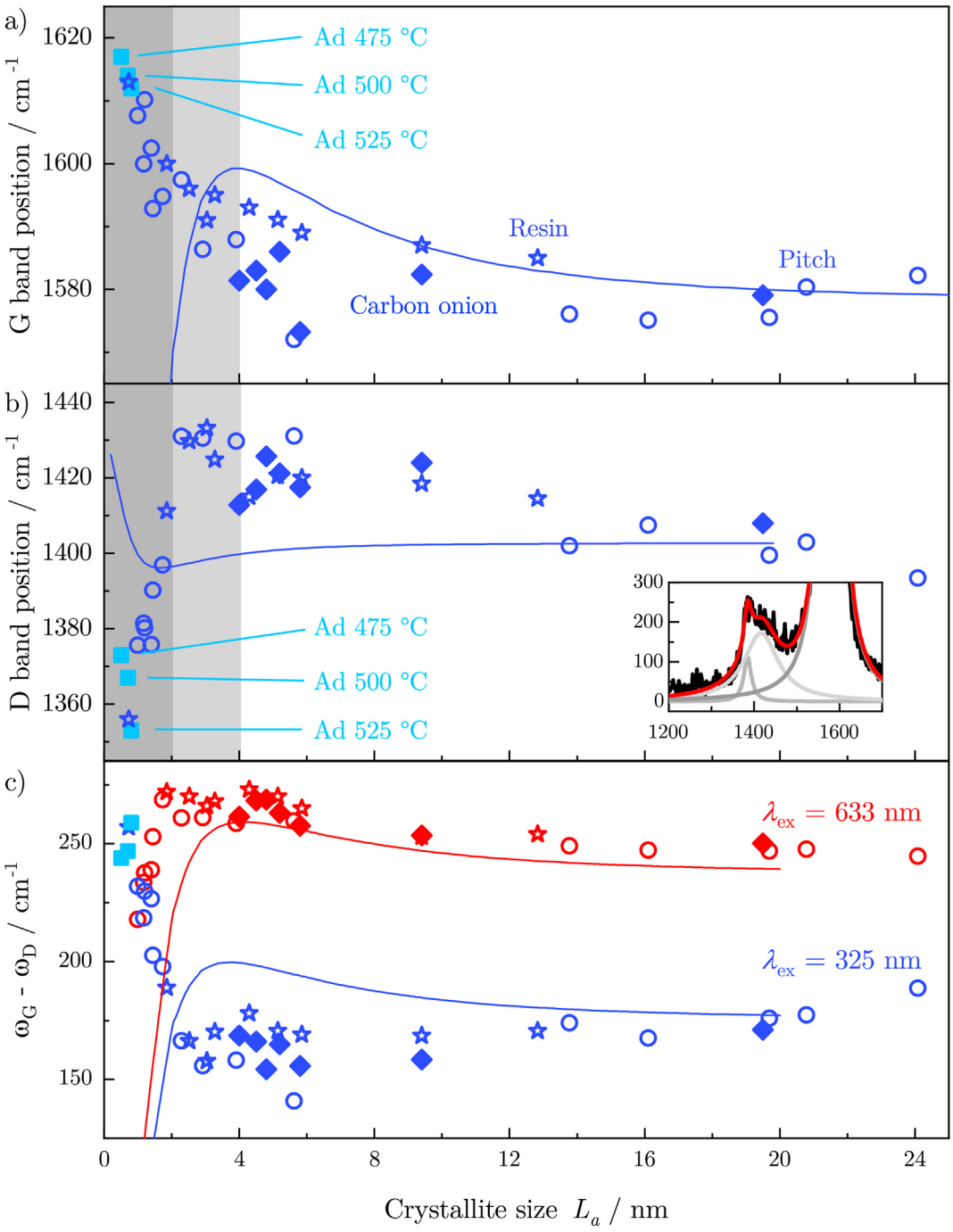

Fig. 4. The G band position in the upper part shows a dependence on the crystallite size L_a for all samples: pitches (circles), resole-based resins (stars), carbon onions (diamonds), and adamantane samples (labeled with Ad, light blue squares). The dependence of the D band positions on nanosheet size L_a is presented in the middle part. All sample series show the same trend. The solid lines are calculated using the Campbell-Fauchet model. The difference between the G and D band $\omega_G - \omega_D$ in the lower part illustrates the behavior of the Raman modes. The data is shown for 633 nm excitation (red color) and for 325 nm excitation (blue color). (A colour version of this figure can be viewed online.)

°C it is about 1612 cm^{-1}. The comparison of the Raman data of the adamantane-based samples with the pitch-based samples is in accordance with L_a values of 0.5 nm, 0.7 nm, and 0.8 nm for the adamantane-based samples heat-treated at 475 °C, 500 °C, and 525 °C, respectively.

The D mode Raman signal of graphene appears as two bands when excited with 325 nm laser light. As an example, the inset in Fig. 4b) shows the D Raman feature of the 2800 °C pitch-based sample of rather large L_a. The two peak-like contributions to the D-signal are clearly visible and may be approximated by one peak located at about 1390 cm^{-1} and another at about 1430 cm^{-1} in this particular case. The reason for the double-peak signal is that the phonons involved in the process are selected by the resonance between laser photon energy and electronic transition energy in the graphene band structure. The description of the band structure of graphene by a symmetric Dirac cone is only valid close to the K (and K′) point. The π and π^* electronic bands yielding the Dirac cone in the vicinity of the K (and K′ point) are asymmetric. This

asymmetry, i.e., the so called trigonal warping effect [48,49], becomes more pronounced with increasing distance from the K (or K′) point in reciprocal space. Thus, when using ultraviolet (UV) light for excitation of the Raman process, the resonance condition for the electronic transition may be fulfilled for different values of $\left|\vec{k}-\vec{k}_{\mathrm{K}}\right|$ and the phonon frequencies $\omega(\vec{k})$ at the selected wavevectors $\vec{k}$ will differ. In this context, $\vec{k}_{\mathrm{K}}$ denotes the wavevector of a K or K' point. As a consequence, the distribution of the different phonon frequencies $\omega(\vec{k})$ selected by the electronic resonance condition leads to a Raman signal of the D mode process, which may be approximated by two peaks. For all samples with L_a values larger than 8 nm, two peaks can be distinguished. However, as L_a decreases, the two peaks merge because their linewidths increase and they cannot be reliably separated by curve fitting anymore. Therefore, we plot in Fig. 4b) the position of the D band extracted from the maximum of the corresponding D Raman signal in the spectra for small L_a and an average of the positions of the two distinguishable maxima of the D Raman signal for larger L_a. Similarly, we take the average of the frequencies derived by theory and plot these values versus L_a as the theoretical curves in Fig. 4b).

The reference samples derived from sp^2-structured resin and pitch precursors and those derived from the sp^3-hybridized adamantane and nanodiamond precursors (the latter only for samples heat-treated at 1100 °C and higher) exhibit the same trend for the D band position vs. L_a in accordance with the findings for the G band position. The nanodiamond-based samples heat-treated at temperatures below 1000 °C do not show any signal in the spectral range of the D band, supporting the view that the Raman band at 1640 cm^{-1} is not G-like. The D-positions extracted from the Raman spectra increase in frequency from about 1400 cm^{-1} for large L_a to 1430 cm^{-1} at $L_a = 2$ nm and then, below 2 nm decrease steeply down to 1350 cm^{-1}. The latter value is still way above the comparatively sharp nanodiamond signal at 1325 cm^{-1} (data points not included in the plot), which dominates the Raman spectra of the samples prepared using the nanodiamond precursors at heat-treatment temperatures below 1000 °C. The theoretical curve does not quite well reproduce the trend observed in the experimental data, which is not surprising considering the complexity of the D-processes and the approximations made. The agreement is reasonable for $L_a > 2$ nm, where the crystalline picture holds but yields the opposite trend for sizes below 2 nm where a molecular description is more appropriate. The position of the D band as a function of L_a derived from Raman spectra obtained with visible excitation light, e.g., 633 nm, is easier to reproduce by the modeling [4]. The reason is that, for laser excitation in the visible range, the resonance condition for the electronic transitions involved occurs at wavevectors, where the Dirac cone as well as the dispersion branches of the phonons involved, are almost of symmetric shape. Thus, only one D Raman band is observed in the Raman spectra for laser excitation in the visible spectral range and the modelling of its position is more straight forward than in case of UV excitation.

A careful analysis of the data in Fig. 4a) and b) reveals that the fluctuations between the experimental data points as well as the deviations between theory and experiment are less pronounced when the difference between G and D band positions is plotted versus L_a. Such plots of the experimental data and corresponding theoretical curves are shown in Fig. 4c) for visible excitation with 633 nm laser light and UV excitation with 325 nm laser light. The theoretical data (solid lines) are close to the experimental data and show the same trend for crystallite sizes $L_a > 4$ nm in both cases. Below 4 nm, the behavior is different for 633 nm and 325 nm excitation. In particular, the modeled curve shows the opposite trend than the experimental data in case of UV excitation whereas, in the case of 633 nm excitation, the modeled differences of the G and D band frequencies follow the trend of the experimental data. However, the theoretical model is expected to fail in this molecule-like size regime. A possible reason for the different behavior of the experimental data points for UV and visible excitation may lie in electronic resonance effects. Excitation in the UV promotes Raman signals of smaller molecule-like structures within the ensemble with average size L_a whose HOMO-LUMO gap is in resonance with the exciting laser [50,51]. Such an influence of the excitation energy on the G band position has been already reported in the literature [52]. Here, the different behavior mainly relates to different trends for the D band position for UV and visible excitation in this range of L_a values, which corresponds to molecule-like units. As the scattering probability of small sp^3-hybridized molecular units with large HOMO-LUMO gap (e.g., diamondoids with $E_{\mathrm{gap}} \geq 6$ eV [53]), which exhibit Raman modes somewhat below the frequency of the D-like modes of sp^2-hybridized molecules (see the Raman spectra in Fig. S4 of SI), is increased compared to that of the sp^2-type molecular units, the different weighing of these signal contributions for the two excitation conditions may cause the different behavior.

A widely used approach for determining the average size L_a of carbons is based on comparing the intensity ratio of D and G-band with empirical master curves, which were gradually refined over the years, e.g., by accounting for its wavelength dependence [35,54–56]. We will discuss the strengths and weaknesses of this approach on the basis of the Raman data obtained from samples prepared from sp^2 and sp^3-based precursors, i.e., pitch, resin, adamantane, and nanodiamond, for two different excitation wavelengths, i.e., 633 nm and 325 nm. The experimental data of $\frac{I_D}{I_G}$ vs. L_a for the four precursors are plotted in Fig. 5. The red and blue data points correspond to 633 nm and 325 nm excitation, respectively. We see that the data points for the two excitation wavelengths are different for all samples and basically define two different curves. The reasons are manifold, but can be subsumed by the keyword Raman resonance. They involve (i) differences in Raman modes and Raman resonance profiles between the various molecular species occurring in the formation process of graphene-like nanosheets in the molecular regime below $L_a < 2$–4 nm including sp^1, and sp^3-structured species (see also Fig. S4 of SI); (ii) even in case of small molecular graphene-like species such as benzene, anthracene, pyrene and coronene consisting of 1, 3, 4, and 7 networked benzene rings, respectively, the Raman cross-section will depend on the excitation wavelengths as the HOMO-LUMO gap varies with size [50,54,57,58]. Thus, the relative contribution to the G and D-like bands in a Raman spectrum of an ensemble of molecular benzene-based species will vary for each species. The same holds for sp^3-type species such as the diamondoids as a function of the number of the adamantane-like units; and (iii) for larger sizes L_a, where the crystalline description of graphene-like nanosheets is valid, a different dependence of the Raman cross-sections of the "real" G and D Raman processes of ideal graphene on excitation wavelength arises mainly from graphene's electronic band structure and phonon dispersion. The main effect visible of this complex interplay of resonance effects and transformation from molecular units to crystal-like units is that the intensity of the D-like Raman mode of the carbons is lower than that of the G-like mode for 325 nm excitation compared to 633 nm excitation.

The two $\frac{I_D}{I_G}$ curves in Fig. 5 increase starting from the smallest L_a and reach a maximum at 2 nm and 4 nm for 325 nm and 633 nm, respectively, and then asymptotically approach zero for infinitely large L_a. However, the maximum occurs at a lower L_a value for 325 nm than for 633 nm excitation. Thus, a simple vertical scaling to a universal excitation-wavelength independent master curve is

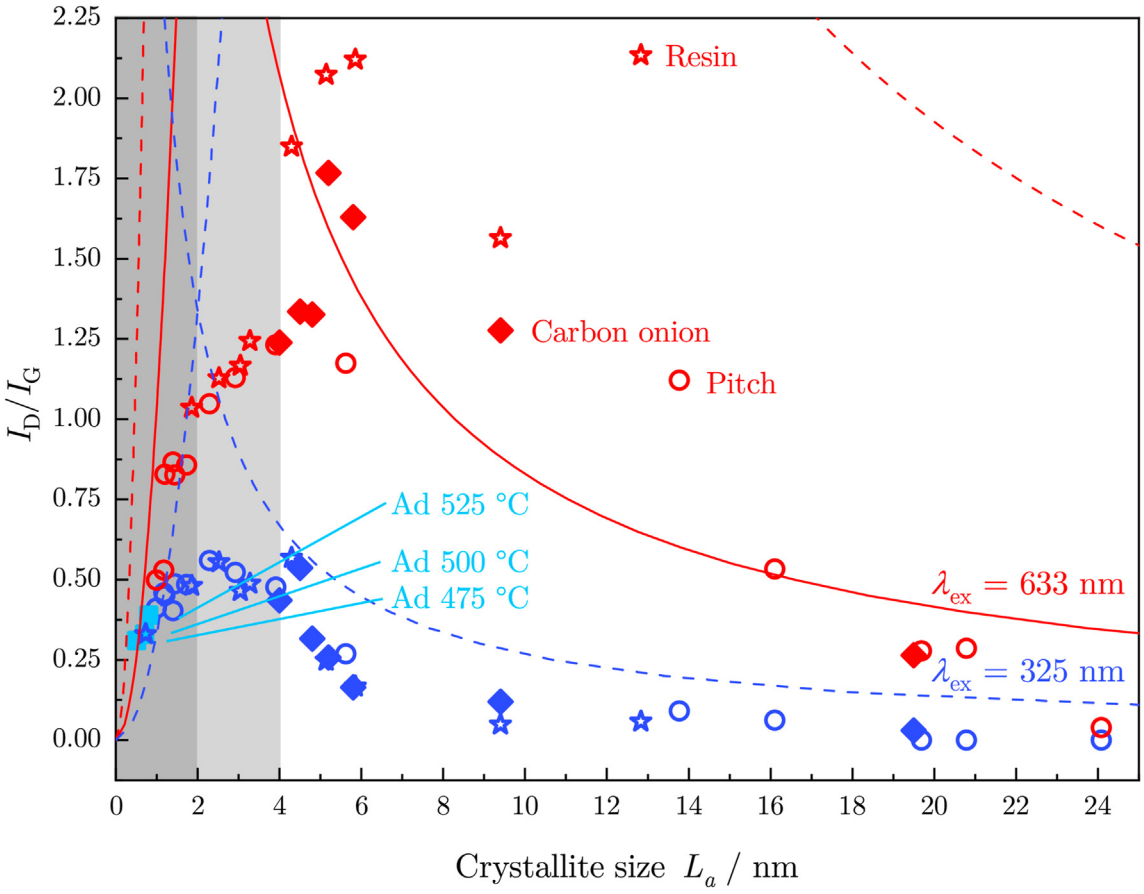

Fig. 5. The intensity ratio of the D and G band $\frac{I_D}{I_G}$ for the four sample series for 633 nm excitation (red color) and for 325 nm excitation (blue color): pitch (circles), resin (stars), carbon onions (diamonds), and adamantane (Ad, light blue squares). Empirical correlations (dashed line: Cançado et al., solid line: Matthews et al.) do not adequately describe the region between L_a = 2 and 4 nm. (A colour version of this figure can be viewed online.)

not possible. It also should be noted that the experimental data of both curves show a pronounced scattering at L_a values somewhat higher than those corresponding to the respective maxima.

The empirically modeling of the $\frac{I_D}{I_G}$ vs. L_a dependence typically applied is not based on a coherent mathematical description, but one approximating the dependence for small sizes (corresponding to the molecular regime) by $\propto L_a^2$ and for large sizes (in the crystal-like regime), which is $\propto L_a^{-1}$. The former is difficult to motivate in the molecular picture on the basis of defect densities simply because the species under consideration are molecules, and a defect in a molecule is not defined. Atomic substitution, a bond rearrangement or bond formation between atomic groups yields another molecule with another well defined vibrational mode spectrum, which may differ in number, mode frequency, and Raman activity from that of the original molecule. As seen in case of adamantane as the precursor, the sharp spectrum of the starting material determined by the sharp modes of one molecular species is transformed into a spectrum representing the superposition of Raman modes of an ensemble of different molecular species with two maxima suggesting a D and G-like Raman band (see also Fig. S4 of SI). Thus, the increase of $\frac{I_D}{I_G} \propto L_a^2$ reflects an increasing number of different molecular species forming during the first intermediate stages of the transformation into a sp^2-hybridized network with average size L_a. This picture is difficult to connect with the crystalline picture used to motivate the L_a^{-1}-dependence for large sizes. The latter is motivated by Raman experiments on large graphene flakes for which a crystalline description of electronic and vibrational states is valid. The Raman microscopic experiments revealed that the D-band is visible only in Raman spectra taken on the edge of the outer circumference of individual graphene flakes [59], i.e. that the edge of the otherwise almost ideal crystalline flake acts as a defect in the D-Raman process. Thus, the magnitude of the D-Raman signal of the entire sample scales with the circumference ($\propto L_a$), whereas the G-Raman signal scales with the area of the flake ($\propto L_a^2$) leading to the L_a^{-1}-dependence for $\frac{I_D}{I_G}$ [35]. A comprehensive model for the transition region between the molecular and crystalline region is not established in the literature and difficult to establish as both models cannot be easily connected.

Curves of $\frac{I_D}{I_G}$ vs. L_a corresponding to the empirical models and based on published parameter sets are plotted as lines in Fig. 5. The dashed and solid lines for $L_a < 2$ nm are based on the empirical formula established by Ferrari and Robertson, i.e., $\frac{I_D}{I_G} \propto L_a^2$ [54], using the prefactors determined by Cançado et al. [56] and Matthews et al. [55], respectively. The same assignment holds for $L_a > 2$ nm, where the dependence proposed by Tuinstra and Koenig, i.e. $\frac{I_D}{I_G} \propto \frac{1}{L_a}$, is used and weighted with those pre-factors. Red and blue colour correspond to 633 nm and 325 nm excitation, respectively, for the pre-factors proposed by Cançado et al. [56]. The formula for deriving the pre-factors given by Matthews et al. is not valid for 325 nm. In the case of 633 nm excitation, the two

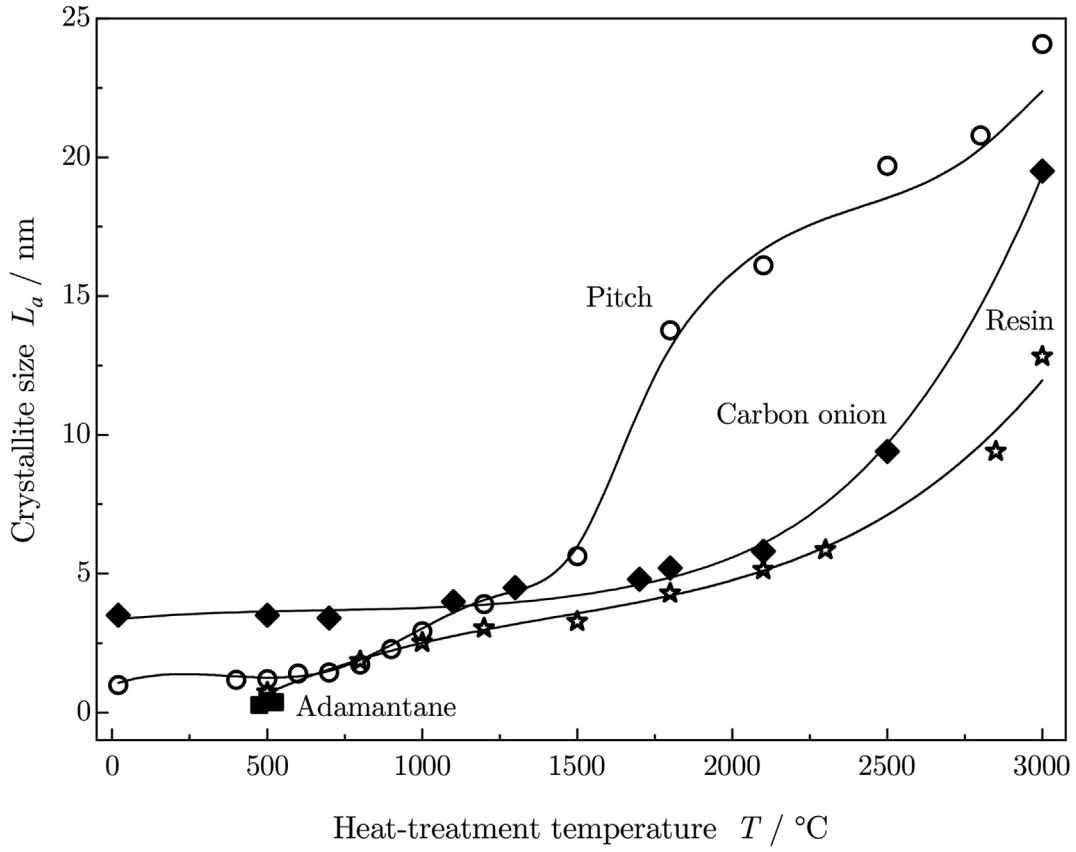

Fig. 6. Average lateral graphene nanosheet size L_a as a function of the heat-treatment temperature T used in the synthesis process of the carbons for various precursor molecules including purely sp^2-hybridized precursors such as resins and pitches as well as nanodiamond as sp^3-type precursor. For the nanodiamond samples at $T \leq 700$ °C the crystallite size of the diamond core is represented, for $T > 700$ °C L_a of the sp^2-structured shell is shown.

parameterizations yield different curves; that by Matthews et al. being in better agreement with the experimental data than that by Cançado et al. However, even the parameterization by Matthews et al. cannot describe the experimental data points well enough to extract reliable L_a values using the model. The experimental data in the transition region from molecule-like to crystal-like, i.e., between 2 nm and 6 nm, cannot be covered by the model. The parameterization by Cançado et al. aligns better with the experimental data for 325 nm excitation than for visible excitation.

It is also of interest to analyse the scattering between the experimental data in more detail and to relate the findings to the type of precursor used and its network forming capabilities. We will mainly focus on the data points obtained with 633 nm excitation because the effects are more pronounced. At very low L_a values up to about 4 nm, the experimental data points of samples derived from the two sp^2-hybridized precursors, i.e., from the soft pitch and resole-based resin, agree quite well for visible as well as UV excitation. The situation for samples derived from the sp^3-type precursors is somewhat different. In the case of the nanodiamond-based samples, the spectra are dominated by nanodiamond Raman signals and, thus, the $\frac{I_D}{I_G}$ can only be extracted for $L_a > 4$ nm. For the adamantane-based samples, the data points for UV excitation of the three samples heat-treated at a temperature of 475 °C and higher, which have started to form sp^2 networks, agree with those of samples of comparable size originating from the sp^2-hybridized precursors. Between $L_a = 4$ and 6 nm, the nanodiamond-based samples as well as the resin-based samples exhibit for 633 nm excitation $\frac{I_D}{I_G}$ ratios, which are much larger than those of pitch-based samples of the same size. At even larger L_a values, the $\frac{I_D}{I_G}$ ratio of the resin-based samples remains large whereas that of the nanodiamond-based samples approaches the values of the pitch-based samples and the corresponding empirically modeled curve based on the parameterization of Matthews et al. These findings can be related to the different network forming properties of the prescursors. Fig. 6 shows the evolution of the lateral size L_a with heat-treatment temperature T in the synthesis process and Fig. S1 of the SI. We showed in our previous publication that carbon materials obtained at the highest heat-treatment temperature of 3000 °C are non-graphitic in case of resin-based samples, whereas pitch-based samples are graphitic [4]. The spectra in Fig. S1 reveal that the nanodiamond-based samples show an intermediate behavior. The sample heat-treated at 2500 °C shows signs of turning graphitic, whereas all others are clearly non-graphitic. In addition, there is a great change in the L_a vs. T curve of the nanodiamond-based samples in Fig. 6 at about 2500 °C from following the data-points of the resin-based samples to following those of the pitch-based samples. In general, we can assume in the crystalline regime at sizes larger than $L_a = 4$ nm, that defects occur as the circumference of the nanosheet formed ($\propto L_a$) as well as, e.g., as point defects in the interior area of the nanosheet ($\propto L_a^2$). The network forming properties not only determine the average size L_a for a given heat-treatment temperature T, but also for a given L_a the defect density within the nanosheet area. For a given size L_a, the contribution of the circumference of the nanosheet to the D-Raman

process can be considered independent of the type of precursor used. In contrast, the area defect density of the nanosheet will strongly depend on the network forming capabilities of the precursor used in the synthesis process. This means that the area contribution to the D mode is almost zero for pitches and considerably larger for resins. In the case of the sp^2-type species formed in the early transformation stages of the nanodiamond precursors into carbon material, this area contribution seems to lie between those of the two sp^2-hybridized precursors. In other words, the network forming properties of the precursor used in the formation process of the carbon material has a major impact on the observed $\frac{I_D}{I_G}$ vs L_a dependence in sample series prepared by varying the heat-treatment temperature.

3.3. Conclusions

In summary, we have demonstrated that sp^2-hybridized carbon materials can be obtained from nanoparticular as well as molecular sp^3-type precursors, i.e., nanodiamonds and adamantane, respectively, by thermal treatment. Raman spectra as a function of heat-treatment temperature T in combination with an average size determination by WAXS, XRD, and TEM reveal that the stages of conversion of an sp^3-hybridized precursor into an sp^2-structured non-graphitic and, at higher temperature, graphitic network in terms of characteristic transformation temperatures depends on the type of precursor used. However, analyzing the transformation as a function of average lateral size L_a of nanostructures formed during synthesis shows that the sp^3-hybridized species transform at lower T (corresponding to small sizes $L_a < 2$ nm) into the sp^2-structured carbon material. At this stage, a variety of different, probably molecular, species form and within this ensemble the fraction of sp^2-hybridized species increases with increasing T. At higher T ($\geq$ 1300 °C corresponding to $L_a > 4$ nm) crystal-like graphene nanosheets are formed by these species, which at the highest heat-treatment temperatures are either non-graphitic (2500 °C) or already graphitic (3000 °C) and show quite sharp reflections in X-ray scattering. The moment D and G-like Raman bands are detectable in the Raman spectra, the analysis of their mode frequencies and intensity ratio as a function of L_a is in good agreement with reference data of samples of comparable size synthesized using sp^2-type precursors, i.e., soft pitches or resole-based resins. In other words, the characteristic Raman features of all samples follow the same trends as a function of average size L_a, to a first approximation, independent of the bonding configuration of the precursor, e.g., the trends in the data points for nanodiamond-based samples lie between those of pitch and resin-based samples in the regime of larger L_a. The differences in the trends exhibited by samples prepared by different precursors reflect the network forming capabilities of the precursor itself as well as the precursor specific intermediate species that arise during the formation of the graphene-like 2D network of the carbon material. These differences in the network forming capabilities of the precursor may be considered the origin of the unreliability of using empirical models solely based on the behavior of D and G-like Raman features for extracting the nanoparticle size L_a. Our results suggest that corresponding master curves for extracting L_a on the basis of Raman spectroscopy may be established when using a defined heat-treatment process using a particular precursor. In such situations, Raman data such as the mode frequencies of D and G bands or their intensity ratio $\frac{I_D}{I_G}$ of a set of reference samples synthesized at different T according to the desired process can be plotted against the average size L_a obtained by an independent structural characterization method to obtain Raman master curves for extracting L_a and to routinely use them for process monitoring.

CRediT authorship contribution statement

Dominique B. Schüpfer: Conceptualization, Validation, Formal analysis, Investigation, Resources, Writing - original draft, Visualization. **Felix Badaczewski:** Formal analysis, Resources, Investigation. **Jan Peilstöcker:** Resources, Investigation. **Juan Manuel Guerra-Castro:** Methodology, Software, Formal analysis. **Hwirim Shim:** Resources, Formal analysis, Validation. **Saleh Firoozabadi:** Resources, Formal analysis, Validation. **Andreas Beyer:** Resources, Formal analysis, Validation. **Kerstin Volz:** Resources, Validation. **Volker Presser:** Conceptualization, Writing - review & editing. **Christian Heiliger:** Conceptualization, Methodology, Writing - review & editing. **Bernd Smarsly:** Conceptualization, Methodology, Writing - review & editing, Supervision. **Peter J. Klar:** Conceptualization, Methodology, Writing - review & editing, Supervision.

Declaration of competing interest

The authors declare that they have no known competing financial interests or personal relationships that could have appeared to influence the work reported in this paper.

Acknowledgement

The authors are grateful for financial support by the Deutsche Forschungsgemeinschaft (DFG) via GRK (Research Training Group) 2204 “Substitute Materials for sustainable Energy Technologies”. Special thanks goes to Marc Loeh, Institute of Physical Chemistry, Justus Liebig University Giessen, Benjamin Krüner, INM - Leibniz Institute for New Materials, Saarbrücken, and Prof. Dr. Klaus Müllen, Max Planck Institute for Polymer Research, Mainz, for the sample preparation. We acknowledge computational resources provided by the HPC Core Facility and the HRZ of the Justus Liebig University Giessen. We would like to thank Dr. Michael Feldmann of HPC-Hessen, funded by the State Ministry of Higher Education, Research and the Arts, for programming advice. We acknowledge funding by the Deutsche Forschungsgemeinschaft in the framework of FOR 2824 “Amorphous Molecular Materials with Extreme Nonlinear Optical Properties”. The INM authors thank Eduard Arzt (INM) for his continuing support.

Appendix A. Supplementary data

Supplementary data to this article can be found online at https://doi.org/10.1016/j.carbon.2020.09.063.

References

[1] P. Adelhelm, K. Cabrera, B.M. Smarsly, On the use of mesophase pitch for the preparation of hierarchical porous carbon monoliths by nanocasting, Sci. Technol. Adv. Mater. 13 (2012), 015010, https://doi.org/10.1088/1468-6996/13/1/015010.

[2] Y.S. Hu, P. Adelhelm, B.M. Smarsly, S. Hore, M. Antonietti, J. Maier, Synthesis of hierarchically porous carbon monoliths with highly ordered microstructure and their application in rechargeable lithium batteries with high-rate capability, Adv. Funct. Mater. 17 (2007) 1873–1878, https://doi.org/10.1002/adfm.200601152.

[3] E. Fitzer, K.H. Köchling, H.P. Boehm, H. Marsh, Recommended terminology for the description of carbon as a solid, Pure Appl. Chem. 67 (3) (1995) 473–506, https://doi.org/10.1351/pac199567030473.

[4] D.B. Schüpfer, F. Badaczewski, J.M. Guerra-Castro, D.M. Hofmann, C. Heiliger, B. Smarsly, Assessing the structural properties of graphitic and non-graphitic carbons by Raman spectroscopy, Carbon 161 (2020) 359–372, https://doi.org/10.1016/j.carbon.2019.12.094.

[5] R. Kumar, S.R. Dhakate, R.B. Mathur, The role of ferrocene on the enhancement of the mechanical and electrochemical properties of coal tar pitch-based carbon foams, J. Mater. Sci. 48 (2013) 7071–7080, https://doi.org/10.1007/s10853-013-7518-z.

[6] K. Jurkiewicz, M. Pawlyta, D. Zygadło, D. Chrobak, S. Duber, R. Wrzalik, et al., Evolution of glassy carbon under heat treatment: correlation

structure–mechanical properties, J. Mater. Sci. 53 (2018) 3509–3523, https://doi.org/10.1007/s10853-017-1753-7.
[7] T. Ko, W. Kuo, Y. Chang, Microstructural changes of phenolic resin during pyrolysis, J. Appl. Polym. Sci. 81 (5) (2001) 1084–1089, https://doi.org/10.1002/app.1530.
[8] E.M. Lotfabad, J. Ding, K. Cui, A. Kohandehghan, W.P. Kalisvaart, M. Hazelton, et al., High-density sodium and lithium ion battery anodes from banana peels, ACS Nano 8 (7) (2014) 7115–7129, https://doi.org/10.1021/nn502045y.
[9] Y. Liu, B. Huang, X. Lin, Z. Xie, Biomass-derived hierarchical porous carbons: boosting the energy density of supercapacitors via an ionothermal approach, J. Mater. Chem. 5 (25) (2017) 13009–13018, https://doi.org/10.1039/C7TA03639F.
[10] J. Cebik, J.K. McDonough, F. Peerally, R. Medrano, I. Neitzel, Y. Gogotsi, et al., Raman spectroscopy study of the nanodiamond-to-carbon onion transformation, Nanotechnology 24 (20) (2013) 1–10, https://doi.org/10.1088/0957-4484/24/20/205703.
[11] G.N. Yushin, S. Osswald, V.I. Padalko, G.P. Bogatyreva, Y. Gogotsi, Effect of sintering on structure of nanodiamond, Diam 14 (10) (2005) 1721–1729, https://doi.org/10.1016/j.diamond.2005.06.030.
[12] M. Zeiger, N. Jäckel, V.N. Mochalin, V. Presser, Review: carbon onions for electrochemical energy storage, J. Mater. Chem. 4 (2016) 3172–3196, https://doi.org/10.1039/c5ta08295a.
[13] O.O. Mykhaylyk, Y.M. Solonin, D.N. Batchelder, R. Brydson, Transformation of nanodiamond into carbon onions: a comparative study by high-resolution transmission electron microscopy, electron energy-loss spectroscopy, x-ray diffraction, small-angle x-ray scattering, and ultraviolet Raman spectroscopy, J. Appl. Phys. 97 (7) (2005), 074302, https://doi.org/10.1063/1.1868054.
[14] D. Weingarth, M. Zeiger, N. Jäckel, M. Aslan, G. Feng, V. Presser, Graphitization as a universal tool to tailor the potential-dependent capacitance of carbon supercapacitors, Adv. Energy Mater. 4 (2014) 1400316, https://doi.org/10.1002/aenm.201400316.
[15] M. Zeiger, N. Jäckel, D. Weingarth, V. Presser, Vacuum or flowing argon: what is the best synthesis atmosphere for nanodiamond-derived carbon onions for supercapacitor electrodes? Carbon 94 (2015) 504–517, https://doi.org/10.1016/j.carbon.2015.07.028.
[16] M.O. Loeh, F. Badaczewski, K. Faber, S. Hintner, M.F. Bertino, P. Mueller, et al., Analysis of thermally induced changes in the structure of coal tar pitches by an advanced evaluation method of X-ray scattering data, Carbon 109 (2016) 823–835, https://doi.org/10.1016/j.carbon.2016.08.031.
[17] W. Ruland, B. Smarsly, X-ray scattering of non-graphitic carbon: an improved method of evaluation, J. Appl. Crystallogr. 35 (2002) 624–633, https://doi.org/10.1107/S0021889802011007.
[18] P. Scherrer, Bestimmung der Größe und der inneren Struktur von Kolloidteilchen mittels Röntgenstrahlen. Nachrichten von der Gesellschaft der Wissenschaften zu Göttingen, Mathematisch-Physikalische Klasse 1918 (1918) 98–100.
[19] P. Giannozzi, S. Baroni, N. Bonini, M. Calandra, R. Car, C. Cavazzoni, et al., Quantum ESPRESSO: a modular and open-source software project for quantum simulations of materials, J. Phys. Condens. Matter 21 (39) (2009) 395502, https://doi.org/10.1088/0953-8984/21/39/395502.
[20] P. Giannozzi, O. Andreussi, T. Brumme, O. Bunau, M.B. Nardelli, M. Calandra, et al., Advanced capabilities for materials modelling with quantum ESPRESSO, J. Phys. Condens. Matter 29 (46) (2017) 465901, https://doi.org/10.1088/1361-648X/aa8f79.
[21] D. Bersani, P.P. Lottici, X.Z. Ding, Phonon confinement effects in the Raman scattering by TiO_2 nanocrystals, Appl. Phys. Lett. 72 (1) (1998) 73–75, https://doi.org/10.1063/1.120648.
[22] P.M. Fauchet, I.H. Campbell, Raman spectroscopy of low-dimensional semiconductors, Crit. Rev. Solid State 14 (sup1) (1988) s79–101, https://doi.org/10.1080/10408438808244783.
[23] J.L. Birman, Theory of Infrared and Raman processes in crystals: selection rules in diamond and zincblende, Phys. Rev. 131 (4) (1963) 1489–1495, https://doi.org/10.1103/PhysRev.131.1489.
[24] S.A. Solin, A.K. Ramdas, Raman spectrum of diamond, Phys. Rev. B 1 (4) (1970) 1687–1698, https://doi.org/10.1103/PhysRevB.1.1687.
[25] K.W.R. Gilkes, H.S. Sands, D.N. Batchelder, W.I. Milne, J. Robertson, Direct observation of sp^3 bonding in tetrahedral amorphous carbon UV Raman spectroscopy, J. Non Cryst. Sol. 227–230 (1) (1998) 612–616, https://doi.org/10.1016/S0022-3093(98)00190-2.
[26] S. Prawer, K.W. Nugent, D.N. Jamieson, J. Orwa, L.A. Bursill, J.L. Peng, The Raman spectrum of nanocrystalline diamond, Chem. Phys. Lett. 332 (1–2) (2000) 93–97, https://doi.org/10.1016/S0009-2614(00)01236-7.
[27] V. Mochalin, S. Osswald, Y. Gogotsi, Contribution of functional groups to the Raman spectrum of nanodiamond powders, Chem. Mater. 21 (2) (2009) 273–279, https://doi.org/10.1021/cm802057q.
[28] J. Speight, Lange's Handbook of Chemistry, 16 ed., McGraw-Hill Education Ltd, 2005, ISBN 9780071432207.
[29] T. Köhler, T. Frauenheim, G. Jungnickel, Stability, chemical bonding, and vibrational properties of amorphous carbon at different mass densities, Phys. Rev. B 52 (16) (1995) 11837–11844, https://doi.org/10.1103/physrevb.52.11837.
[30] D.A. Drabold, P.A. Fedders, P. Stumm, Theory of diamondlike amorphous carbon, Phys. Rev. B 49 (23) (1994) 16415–16422, https://doi.org/10.1103/PhysRevB.49.16415.
[31] K.W.R. Gilkes, H.S. Sands, D.N. Batchelder, J. Robertson, W.I. Milne, Direct observation of sp^3 bonding in tetrahedral amorphous carbon using ultraviolet Raman spectroscopy, Appl. Phys. Lett. 70 (15) (1997) 1980–1982, https://doi.org/10.1063/1.118798.
[32] A.C. Ferrari, Determination of bonding in diamond-like carbon by Raman spectroscopy, Diam. Relat. Mater. 11 (3–6) (2002) 1053, https://doi.org/10.1016/S0925-9635(01)00730-0.
[33] V.Y. Osipov, A.V. Baranov, V.A. Ermakov, T.L. Makarova, L.F. Chungong, A.I. Shames, et al., Raman characterization and UV optical absorption studies of surface plasmon resonance in multishell nanographite, Diam. Relat. Mater. 20 (2) (2011) 205–209, https://doi.org/10.1016/j.diamond.2010.12.006.
[34] R. Pfeiffer, H. Kuzmany, P. Knoll, S. Bokova, N. Salk, B. Günther, Evidence for trans-polyacetylene in nano-crystalline diamond films, Diam. Relat. Mater. 12 (3–7) (2003) 268–271, https://doi.org/10.1016/S0925-9635(02)00336-9.
[35] F. Tuinstra, J.L. Koenig, Raman spectrum of graphite, J. Chem. Phys. 53 (3) (1970) 1126–1130, https://doi.org/10.1063/1.1674108.
[36] R. Vidano, D.B. Fischbach, New lines in the Raman spectra of carbon and graphite, J. Am. Ceram. Soc. 61 (1–2) (1978) 13–17, https://doi.org/10.1111/j.1151-2916.1978.tb09219.x.
[37] A. Jorio, R. Saito, G. Dresselhaus, M.S. Dresselhaus, Raman Spectroscopy in Graphene Related Systems, WILEY-VCH Verlag GmbH & Co. KGaA, 2011, ISBN 978-3-527-40811-5.
[38] L.M. Malard, M.A. Pimenta, G. Dresselhaus, M.S. Dresselhaus, Raman spectroscopy in graphene, Phys. Rep. 473 (5–6) (2009) 51–87, https://doi.org/10.1016/j.physrep.2009.02.003.
[39] L.G. Cançado, M.A. Pimenta, R. Saito, A. Jorio, L.O. Ladeira, A. Grueneis, et al., Stokes and anti-Stokes double resonance Raman scattering in two-dimensional graphite, Phys. Rev. B 66 (3) (2002), 035415, https://doi.org/10.1103/PhysRevB.66.035415.
[40] L. Cançado, K. Takai, T. Enoki, M. Endo, Y. Kim, H. Mizusaki, et al., Measuring the degree of stacking order in graphite by Raman spectroscopy, Carbon 46 (2) (2008) 272–275, https://doi.org/10.1016/j.carbon.2007.11.015.
[41] L.G. Cançado, A. Reina, J. Kong, M.S. Dresselhaus, Geometrical approach for the study of G' band in the Raman spectrum of monolayer graphene, bilayer graphene, and bulk graphite, Phys. Rev. B 77 (24) (2008b) 245408, https://doi.org/10.1103/PhysRevB.77.245408.
[42] A.C. Ferrari, J.C. Meyer, V. Scardaci, C. Casiraghi, M. Lazzeri, F. Mauri, et al., The Raman fingerprint of graphene, Phys. Rev. Lett. 97 (2006) 187401, https://doi.org/10.1103/PhysRevLett.97.187401.
[43] I.H. Campbell, P.M. Fauchet, The effects of microcrystal size and shape on the one phonon Raman spectra of crystalline semiconductors, Solid State Commun. 58 (10) (1986) 739–741, https://doi.org/10.1016/0038-1098(86)90513-2.
[44] C. Castiglioni, C. Mapelli, F. Negri, G. Zerbi, Origin of the D line in the Raman spectrum of graphite: a study based on Raman frequencies and intensities of polycyclic aromatic hydrocarbon molecules, J. Chem. Phys. 114 (2) (2001) 963–974, https://doi.org/10.1063/1.1329670.
[45] R. Meinke, R. Richter, A. Merli, A.A. Fokin, T.V. Koso, V.N. Rodionov, et al., UV resonance Raman analysis of trishomocubane and diamondoid dimers, J. Chem. Phys. 140 (2014), 034309, https://doi.org/10.1063/1.4861758.
[46] R.F. Egerton, M.J. Whelan, Electron energy loss spectra of diamond, graphite and amorphous carbon, J. Electron. Spectrosc. Relat. Phenom. 3 (3) (1974) 232–236, https://doi.org/10.1016/0368-2048(74)80015-0.
[47] A. Oya, H. Nakamura, S. Otani, H. Marsh, Carbonization of adamantane to a graphitizable carbon, Fuel 60 (8) (1981) 667–669, https://doi.org/10.1016/0016-2361(81)90215-5.
[48] J. Kürti, V. Zólyomi, A. Grüneis, H. Kuzmany, Double resonant Raman phenomena enhanced by van Hove singularities in single-wall carbon nanotubes, Phys. Rev. B 65 (2002) 165433, https://doi.org/10.1103/PhysRevB.65.165433.
[49] R. Saito, G. Dresselhaus, M.S. Dresselhaus, Trigonal warping effect of carbon nanotubes, Phys. Rev. B 61 (4) (2000) 2981–2990, https://doi.org/10.1103/PhysRevB.61.2981.
[50] S. Müller, K. Müllen, Expanding benzene to giant graphenes: towards molecular devices, Phil. Trans. R. Soc. A 365 (2007) 1453–1472, https://doi.org/10.1098/rsta.2007.2026.
[51] J. Robertson, Amorphous carbon, Adv. Phys. 35 (4) (1986) 317–374, https://doi.org/10.1080/00018738600101911.
[52] A.C. Ferrari, J. Robertson, Resonant Raman spectroscopy of disordered, amorphous, and diamondlike carbon, Phys. Rev. B 64 (2001), 075414, https://doi.org/10.1103/PhysRevB.64.075414.
[53] L. Landt, K. Klünder, J.E. Dahl, R.M.K. Carlson, T. Möller, C. Bostedt, Optical response of diamond nanocrystals as a function of particle size, shape, and symmetry, Phys. Rev. Lett. 103 (4) (2009), 047402, https://doi.org/10.1103/PhysRevLett.103.047402.
[54] A.C. Ferrari, J. Robertson, Interpretation of Raman spectra of disordered and amourphous carbon, Phys. Rev. B 61 (20) (2000) 14095–14107, https://doi.org/10.1103/PhysRevB.61.14095.
[55] M.J. Matthews, M.A. Pimenta, G. Dresselhaus, M.S. Dresselhaus, M. Endo, Origin of dispersive effects of the Raman D band on carbon materials, Phys. Rev. B 59 (10) (1999) 6585–6588, https://doi.org/10.1103/PhysRevB.59.R6585.
[56] L.G. Cançado, K. Takai, T. Enoki, M. Endo, Y.A. Kim, H. Mizusaki, et al., General equation for the determination of the crystallite size L_a of nanographite by Raman spectroscopy, Appl. Phys. Lett. 88 (16) (2006) 163106, https://doi.org/10.1063/1.2196057.
[57] M. Chhowalla, A.C. Ferrari, J. Robertson, G.A.J. Amaratunga, Evolution of sp^2

bonding with deposition temperature in tetrahedral amorphous carbon studied by Raman spectroscopy, Appl. Phys. Lett. 76 (11) (2000) 1419–1421, https://doi.org/10.1063/1.126050.
[58] J. Robertson, E.P. O'Reilly, Electronic and atomic structure of amorphous carbon, Phys. Rev. B 35 (6) (1987) 317–374, https://doi.org/10.1103/PhysRevB.35.2946.
[59] M.A. Pimenta, G. Dresselhaus, M.S. Dresselhaus, L.G. Cançado, A. Jorio, R. Saito, Studying disorder in graphite-based systems by Raman spectroscopy, Phys. Chem. Chem. Phys. 9 (2007) 1276–1290, https://doi.org/10.1039/b613962k.